Cubically symmetric mechanical metamaterials projected from 4^{th} dimensional geometries reveal high specific properties in shear

Gabrielis Cerniauskas[a], Parvez Alam[a,*]

[a]*School of Engineering, The University of Edinburgh, Edinburgh, UK*

Abstract

Reduced density significantly compromises the mechanical properties of ordinary materials as their structural components undergo bending when subjected to shear loading. In this paper, we present an emerging class of cubically symmetric mechanical metamaterial, based on 3-space geometrical shadows of 4^{th} dimensional geometries (4-polytopes) that are optimised for high shear resistance and minimised weight. We show that by employing a genetic algorithm-based optimisation framework, the mechanical metamaterials can achieve an increase of more than 40-fold in their specific shear properties. Experimental results reveal that the metamaterial structure with the highest specific shear resistance, the 5-cell (pentatope), exhibits specific shear stiffness that is almost 2-fold higher than that of a gyroid, while the 8-cell (tesseract) structure exhibits the highest specific shear yield strength that is 2.4 times higher than that of a hexagonal honeycomb tested in the out-of-plane direction.

Keywords: Shear loading, Genetic Algorithm, Mechanical Metamaterial, Cellular Solids, 3D printing, Parametric Optimisation

1. Introduction

Mechanical metamaterials have received significant attention in recent years since their, often extraordinary, properties and behaviours can be engineered by varying the geometries of their architectures. Recent advancements in additive manufacturing technologies have enabled higher levels of manufacturing complexity in cellular solids, and as such, there is an increase in the potential for their application in diverse areas such as aerospace, automotive and biomedical [1]. The ability to alter the architecture alongside the constituent material properties and relative densities of cellular solids enables the engineering of enhanced mechanical responses, which in some cases surpasses the natural behaviour of the bulk constituent [2]. A few examples that can be used to demonstrate the breadth of potential in designing novel mechanical metamaterials include lightweightness [3, 4, 5], variable stiffness [6, 7, 8] and structures with near-zero or even negative Poisson's ratio [9, 10, 11].

While the majority of research to date concerns the axial loading of mechanical metamaterials, there have been far fewer efforts that have considered shear loading. Yet, shear loading is ubiquitous in engineered structures and an aim should be to more commonly factor shear into the design process of novel mechanical metamaterials. From amongst the papers that have considered shear loading, pentamode structures are interesting [12] as they exhibit a vanishing shear modulus, i.e. these are solids that behave like fluids in that they are difficult to compress yet easy to deform [13, 2, 14, 15]. As such, the 'highly rubbery' behaviour of pentamode structures has been found to be useful in a wide range of applications varying from 3D-printed shoes [2] to seismic isolation devices [16]. Other unusual metamaterial properties in shear include inducing coupling effects between normal strain and shear [17, 18, 19, 20], which can usually be achieved through chiral architectures [21], or structures that absorb [22, 23] and dissipate energy in shear [24, 25]. There are only a limited number of papers that focus on enhancing the shear properties of metamaterials, with some demonstrating high shear stiffness of lattices [26, 27, 28] and thin-wall-based structures [29, 27, 30]. A common

*Corresponding author
Email addresses: g.cerniauskas@ed.ac.uk (Gabrielis Cerniauskas), parvez.alam@ed.ac.uk (Parvez Alam)

practice is to incorporate computational design with finite element analyses [3, 4, 6, 9, 10, 11, 13, 31] to accelerate the development of new metamaterials. These methods are also often accompanied by various optimisation frameworks employing machine learning [28, 32] or meta-heuristic search algorithms such as gradient-descent [33, 34, 35], nature-inspired algorithms [13, 36, 37], Bayesian methods [38, 39, 40] and neural networks [11, 41, 42, 43, 44]. Recent publications suggest that new breakthroughs in machine learning have potential in effectively solving complex design problems, which were previously not possible [41, 45]. These techniques are usually employed to perform parametric [15, 17, 42] or topology optimisation [14, 13] as well as multiscale optimisation [46, 47, 48], as a part of surrogate models [44, 47] or inverse design frameworks [11, 41, 42, 43].

Building on our previous work [49, 50], the work presented here further investigates 3D projected 'shadows' of 4^{th} dimensional polytopes (4-polytopes), which in our previous work have been shown to possess excellent specific mechanical properties as the projected shadows comprise quasi-fractal structural hierarchies [4, 51, 52, 42, 53]. 4-polytope projected 3D mechanical metamaterials comprise self-repeating geometries, taking advantage of numerous symmetry planes within the projected 4-polytope unit cell. Consequently, these structures hold significant promise in applications where there is a demand for both high stiffness and lightweightness. In this paper, we employ Schlegel wire-frame diagrams to generate 3D metamaterials based on regular 4-polytopes (4^{th} dimensional geometries), namely 5-cell (pentatope), 8-cell (tesseract), 16-cell (orthoplex) and 24-cell (octaplex). We investigate their resistance to shear loading and use meta-heuristic optimisation approaches to maximise their specific shear stiffness properties. Finally, we investigate how optimising the shear stiffness affects other mechanical properties, providing a more in-depth understanding of this new class of mechanical metamaterial.

2. Methodology

2.1. Design of 4-polytope-based unit cells

Four varieties of 4-polytopes namely, 5-cell (pentatope), 8-cell (tesseract), 16-cell (orthoplex) and 24-cell (octaplex), were considered as base structures for metamaterial design. As shown in Figure 1 (a), these 4^{th} dimensional structures can be represented as 'shadows' in 3-space using Schlegel diagrams. Fundamentally, the Schelgel method creates a central projection to to elucidate the symmetries of the 4-polytope structure in 3-space. Thus the structure is reduced from a 4D to a 3D geometry via a single perspective of the 4-polytope, and we render this as an initial wire-frame structure. These 3D projections were then used to develop the metamaterial unit cells by considering the edges and vertices of the wire-frames as contours for thin-walled unit cell structures illustrated in Figure 1 (b). The wire-frames represent spatial coordinates in 3-space rather than actual solid structures. The thin-walled unit cell structures were designed as extensions from these wire-frames, which defined the boundaries of the 3D projected 4-polytopes. The 4-polytope-based unit cells were built up using the wireframe as silhouettes. This was to guarantee that the thin-walled structures maintain the same symmetry planes as the 4-polytopes projections, thereby ensuring all unit cells were cubically symmetrical (i.e. with same geometrical arrangement along three orthogonal principal axes). Using this approach allowed for the adjustment of solid features within each unit cell, whilst maintaining the core geometrical aspects of a 3D projected 4-polytope. This therfore additionally allowed for the parametrisation of the unit cell structures as presented in Figure 2 and which are also listed as design parameters in Table 1. Introducing thin-walled features that can be modified thus allowed for the generation of multiple unit cell geometries that originate from the same 4-polytope projection and hence, the same symmetry planes could be maintained throughout the optimisation process. For example, the perspective depth of each 4-polytope-based unit cell can be adjusted by enlarging or shrinking the internal geometrical features, such as the inner cube in the 8-cell structure, while maintaining a geometrical definition of a 3D projected 4-polytope. As such, changes to the structure in this way will affect the mechanical properties of the unit cell, which enables tailoring of metamaterial properties to suit a specific mechanical objective.

As a part of this design process, certain features were incorporated in the unit cell structures to account for the manufacturing requirements and limitations (further described in Section 2.4). These features were included to allow circulation of 3D printing resin within the structure. The design parameter limits were set to ensure the manufacturability of the structures while the exterior dimensions of the unit cells were set to constant by using a cubical bounding volume with an edge length of 15 mm. Defining the unit cell structures in this way ensured that the design process could be iterated and automated to generate numerous geometrical arrangements most suited to respond

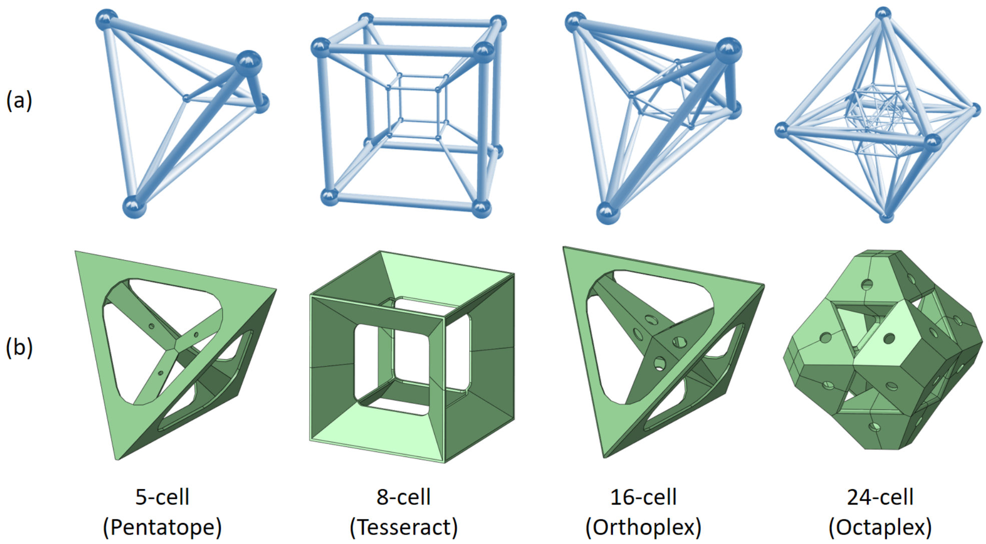

Figure 1: (a) Schlegel wire-frame diagrams of 4-dimensional regular convex polytopes (4-polytopes) and (b) 3D projected 4-polytope thin-walled unit cells based on the wire-frame diagrams.

to the external loading while also stacking the unit cells together to form manufacturable mechanical metamaterial arrays.

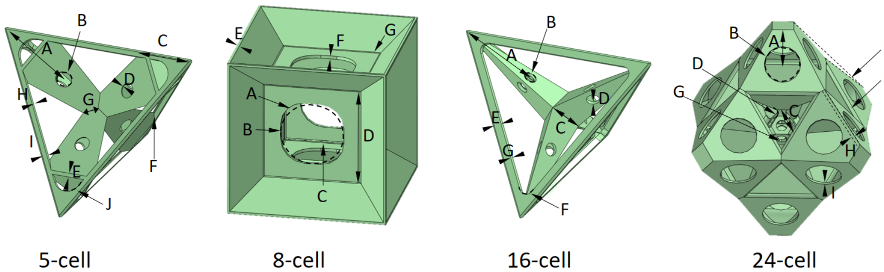

Figure 2: Parametric design approach to 4-polytope projected metamaterial design. Adjustable parameters are marked in letters for each structure. Figure adapted from [49]

.

2.2. *Modelling of unit cells*

Computational modelling work was carried out to characterise the mechanical response of the 4-polytope projections as unit cells under shear loading. Commercially available finite element analysis software (Abaqus by Dassault Systémes) was used to build elasto-plastic shear deformation models. Material properties were set up to mimic the mechanical properties of the fully cured 3D printing resin (Clear V4 by Formlabs) with Young's modulus value of 2.03GPa, Poisson's ratio of 0.38 and density of 1.164g/cm^3. The yield stress (τ_y) value was set to 72.28 MPa and the strain softening behaviour in the plastic part of the stress-strain curve was approximated using a power trendline defining shear stress and strain (ϵ_y) relationship as $\tau_y = 44.99 \times \epsilon_y^{-0.142}$.

The metamaterial unit cells were discretised using a free meshing approach which is more suitable and reliable for automated remeshing of the structures when compared with swept and structured discretisation techniques. Tetrahedral mesh elements (C3D10) were used. A mesh convergence study was carried out to determine the most optimal

Table 1: Parametric design variables for 5, 8, 16 and 24-cell designs as illustrated in Figure 2. Table adapted from [49].

5-cell		8-cell		16-cell		24-cell	
A	Drain hole distance	A	Drain hole round radius	A	Drain hole distance	A	Drain hole distance
B	Drain hole radius	B	Drain hole radius	B	Drain hole radius	B	Drain hole radius
C	Corner distance	C	Inner edge round radius	C	Inner triangle size	C	Inner triangle size
D	Inner wall thickness	D	Inner cube size	D	Inner wall thickness	D	Inner triangle round
E	Corner wall thickness	E	Outer wall thickness	E	Outer shell width	E	Projection angle
F	Outer corner round	F	Inner cube wall thickness	F	Outer shell round	F	Outer shell round
G	Inner triangle size	G	Outer edge round radius	G	Outer shell width	G	Inner wall thickness
H	Outer shell thickness					H	Middle wall thickness
I	Outer shell width					I	Outer wall thickness
J	Outer shell round						

meshing density for each 4-polytope-based unit cell. A meshing rule was incorporated into the discretisation procedure such that there would be a minimum of three elements across the thinnest feature of the structure, with the number of elements increasing from this as the feature thickens. To ensure even sizing of the elements throughout the discretised geometry, a mesh growth rate value was set to 1.05. The discretisation approach described here ensures that the mesh is fine enough to capture the through-thickness behaviour of the thin-walled structures, while generating a minimum number of mesh elements required for an accurate computational solution.

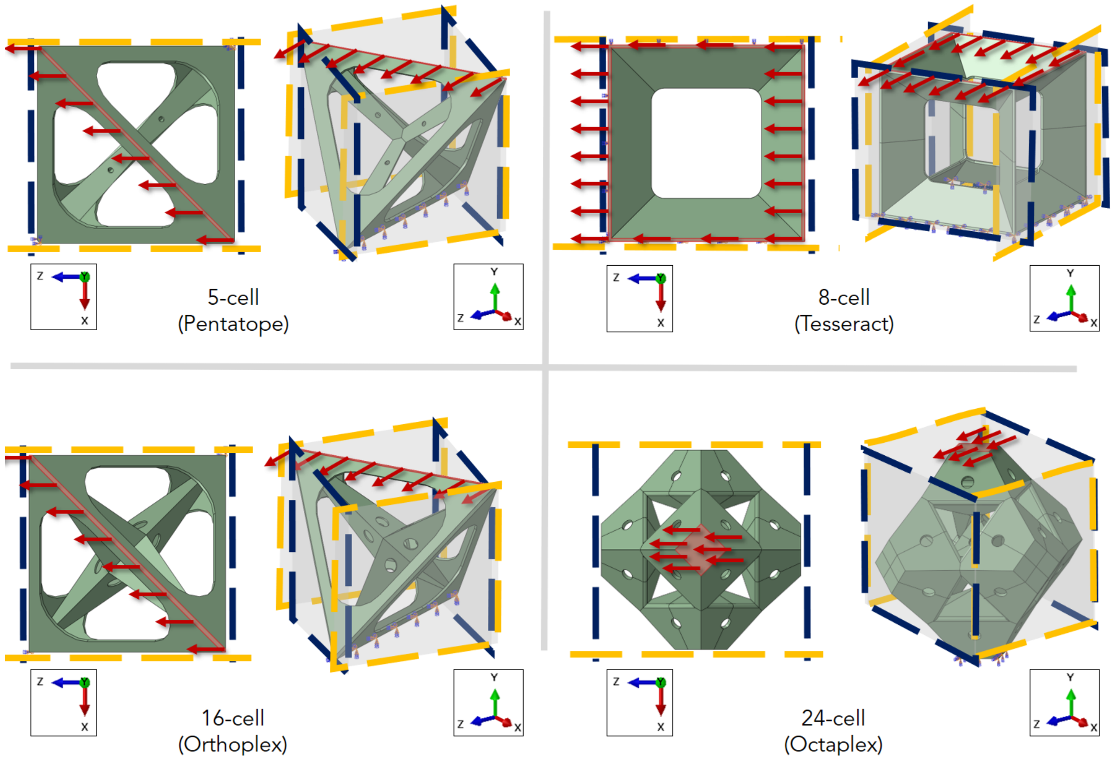

Figure 3: Summary of the boundary conditions applied to the unit cells developed for the shear set loading conditions. A full unit cell was simulated with the two X planes (marked in yellow dashed line) representing the periodic boundary conditions, while the bottom and the top of the cell are prescribed an encastre and a shear loading condition respectively. The diagram shows the top view of each unit cell on the left and a perspective view on the right.

Full unit cell geometries were simulated for each 4-polytope projection to capture the response to shear loading conditions. An Encastre boundary condition was applied to the bottom of each unit cell, while a shear displacement in the direction parallel to the outermost surface was applied at the top of the unit cell. The displacement value was set to result in an overall unit cell shear strain of 0.10. As shown in Figure 3, symmetric boundary conditions were applied to the outermost unit cell surfaces which are perpendicular to the x-axis, marked in yellow. Periodic boundary conditions, marked in dark blue, were applied to the outermost surfaces perpendicular to the z-axis. Periodic boundary conditions captured the forces and deformation that an adjacent unit cell could impose on the simulated unit cell. Symmetric instead of periodic boundary conditions were implemented on the surfaces marked in yellow dashed lines as applying them to the surfaces parallel to the shear loading direction (1) did not alter simulation outputs and (2) reduced computational time. These boundary conditions are representative of a unit cell located inside a metamaterial array and surrounded by adjacent cells of the same type. The Newton-Raphson method implemented within the Abaqus Implicit solver was used to analyse the structures as it was found to be well suited to the problem. This approach enabled the use of variable time increments whilst maintaining high simulation accuracy and significantly reducing computational time.

2.3. Parametric optimisation approach

The 4-polytope projected unit cells presented thus far were designed without any insight into how these structures behave under shear loading. To address this and to enhance the performance of the existing designs, we employed a parametric optimisation method. Parametric design variables defining the geometrical features of the unit cells (Table 1) were set as inputs to the optimisation algorithm, which in an automated fashion iteratively adjusted the variables and generated a set new unit cell designs. These were then analysed using the finite element model described in Section 2.2. The results from each simulation were then post-processed and fed to the optimisation algorithm to be ranked against other designs and hence provided machine training for parameter selection in consecutive design iterations. Additionally, manufacturing constraints were incorporated into this computational design task to avoid exploring structures that could not be fabricated. The two implemented constraints stem from the limitations of the low force stereolitography (LFS) process, further discussed in Section 2.4, and are namely: (1) lower wall thickness limit and (2) lower limit for a drain hole diameter. The former is dictated by the minimum force required to peel the printed part from the resin tank while the latter is limited by the viscosity of the resin and must be incorporated to ensure a sufficient flow rate while draining the hollow chambers within the unit cell structure. As a result, the features that are too small to produce or the ones that would result in suction cups (concave geometrical features preventing the free flow of resin) were not evaluated during the process of optimisation. Specified ranges of design variables and the final values for optimised structures are provided as Electronic Supplementary Table 1.

The objective function aimed to maximise the specific shear stiffness, $\frac{G}{\rho}$, where G is the shear modulus of the unit cell and ρ is the apparent density of the unit cell. The optimisation framework was built by combining the finite element simulation set-up with a meta-heuristic evolutionary algorithm using FE results to explore the performance of metamaterial unit cells with different parametric design variable inputs (Table 1). At each iteration, a single metamaterial unit cell was generated and analysed using the FE method to obtain the total elastic strain energy, U_g resultant from shear loading, and the unit cell mass, m, values as performance-indicating measures. The optimisation algorithm then uses this information to find the structure exhibiting the highest specific shear stiffness, which is formulated in Equation 1, where V is the total volume of the unit cell, τ_{total} is the total shear stress from shear loading of the complete unit cell.

$$\frac{G}{\rho} = \left(\frac{\tau_{total}^2 V}{2U_g}\right)\left(\frac{m}{V}\right)^{-1} \tag{1}$$

$$U_g = \sum_{e=1}^{n} V_e \cdot \frac{1}{2}\int_0^{\gamma_{ij}} \tau_{ij} d\gamma_{ij} + \sigma_{ij} d\epsilon_{ij} \tag{2}$$

To avoid using brute force searching methods, a single objective genetic algorithm (GA) was tasked to search for correlation between the input design parameters and the performance measures. This approach allowed for the exploration of a multi-dimensional design space in an efficient manner and to arrive at a near-optimum design solution while minimising the computational expenses. The objective function formulated for the optimisation process (shown in Equation 1) was based on the total elastic strain energy resulting from shear forces, U_g, as demonstrated by Equation

2, where V_e is the volume of a single mesh element, n is the number of mesh elements, τ_{ij} and γ_{ij} are the elastic shear stress and elastic shear strain tensors of a mesh element, respectively, and σ_{ij} and ϵ_{ij} are the elastic normal stress and elastic normal strain tensors of a mesh element, respectively. As the algorithm proceeds, it generates structures which with each iteration have a higher specific shear stiffness ($\frac{G}{\rho}$) as they are based on the previous search knowledge. This is achieved by selecting the best-performing unit cells from the previous runs and using mutation and crossover actions to generate a new population of structures. The new designs are evaluated using the finite element model and the outputs are fed back into the genetic algorithm. The procedure is repeated multiple times until the stopping criterion is met and then the best existing unit cell design is chosen as the near-optimum solution. A schematic representation of the algorithm is shown in Figure 4.

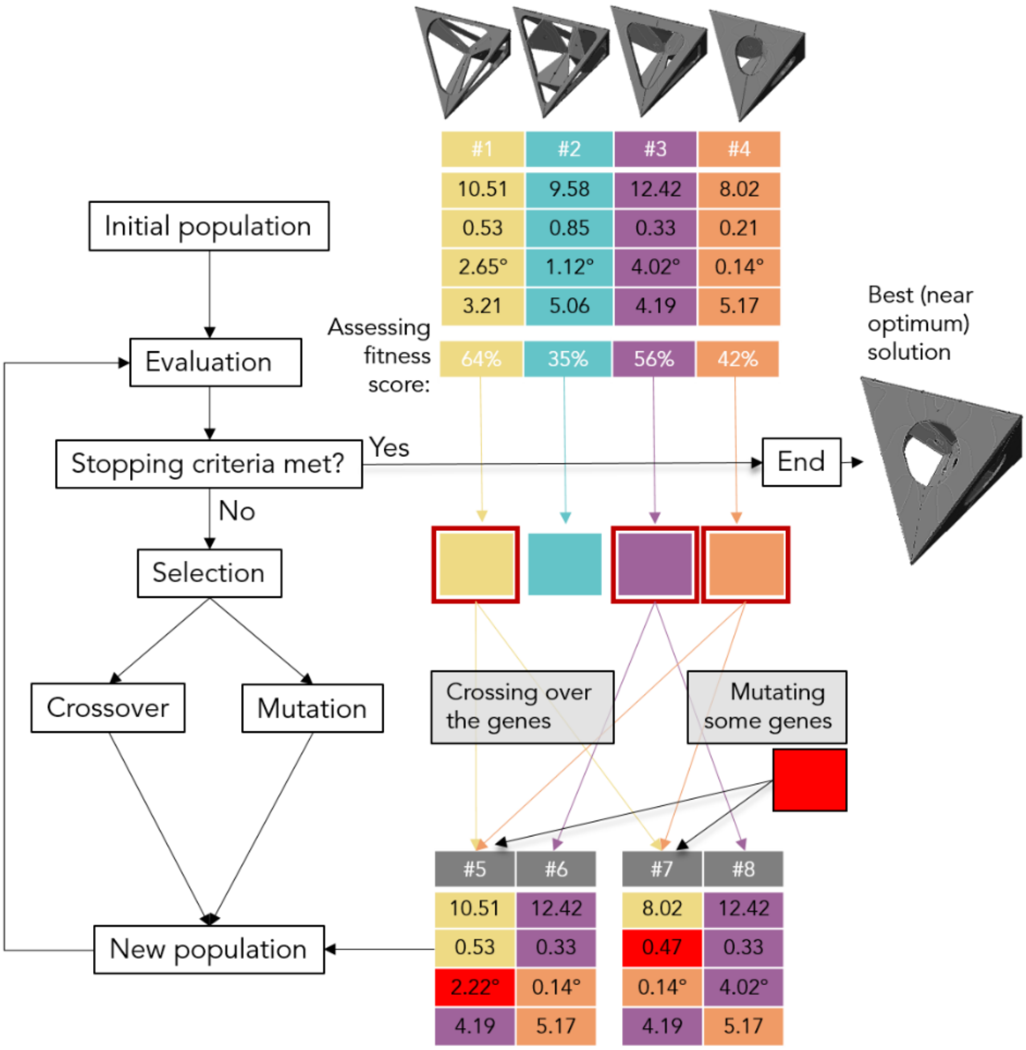

Figure 4: Schematic representation of genetic algorithm used in the optimisation framework.

The genetic algorithm uses a population size of 16, the choice of which was based on the finite element simulation size for a shear loading scenario and the available computing resources that allowed 16 simulations to be executed in parallel. The maximum number of generations was not limited in this optimisation problem, however, a stopping criteria was built in to terminate the process when the performance results of the newly generated structures showed no improvement over the following 20% of the total executed generations (counting from the best existing solution). Such a criterion was chosen to not only stop the optimisation process but to also reduce the design time and the associated computational costs when a suitable unit cell design is found. It should also be noted that all of the four 3D projected 4-polytope unit cells reached the stopping criteria in under 704 iterations. Crossover and mutation probabilities were set to 0.9 and $1/q$ respectively, where q is the number of design variables, summarised in Table 2. Crossover and mutation indices were chosen as 10 and 20, respectively, while the GA parameter tuning was not performed as it was deemed to be beyond the scope of this study. The values listed here were selected based on previously available knowledge for a similar mechanical metamaterial design optimisation problem reported in [49].

Table 2: Summary of the parameters used in genetic algorithm set-up, [49].

GA parameters:	
Population size	28
Crossover probability	0.9
Mutation probability*	1/q
Crossover distribution index	10
Mutation distribution index	20
Stopping criteria	no improvement in last 20% of gen.

*q is the number of design variables

2.4. Manufacturing methods

The specimens were designed using the unit cells optimised to exhibit high specific stiffness under shear loading (boundary conditions presented in Section 2.2). The experimental shear samples were manufactured using Form 3 desktop 3D printers by Formlabs which employ low force stereolithography (LFS) additive manufacturing technology. Photoreactive thermosetting Clear V4 resin compatible with this 3D printing method was used for prototyping and the samples were printed using a layer height of 25µm. Following this process, isopropyl alcohol was used to wash the specimens and remove excess resin within the internal cavities of the metamaterial structures. The samples were then further post-processed using a Form Cure UV light chamber for the duration of 30 min to fully cure the 3D printed resin and hence increase the stiffness and strength of the material. The unit cell arrangement was chosen as $2 \times 2 \times 8$ to provide a sample with the size required for the mechanical testing procedure while fitting the maximum size specimen within the build volume of the 3D printer. This resulted in a set of samples with 32 unit cells and external dimensions of $30 \times 30 \times 120$ mm. The linear dimensional accuracy was evaluated by comparing the experimental samples with the CAD models and the specimens were found to have high dimensional accuracy with a deviation of less than 0.38%. The specimen mass was found to be consistent among the 3D-printed samples of the same metamaterial structure, however, the mass variation, Δw, between the computationally designed models and experimental samples was found to be 5.34%, 7.90%, 5.06% and 9.10% for the 5-cell, 8-cell, 16-cell and 24-cell samples, respectively. The mass variation was calculated as $\Delta w = \left(\frac{w_{sample}}{w_{CAD}} - 1\right)$, where w_{sample} is the measured mass of a 3D printed and post-cured metamaterial sample and w_{CAD} is the mass of the same sample calculated using the volume of the structure's CAD model and the density of the fully cured 3D printing resin. The main reason for this mass variation is due to the excess resin remaining within the internal geometry of the specimen after the washing procedure is completed. During the post-curing process, excess resin polymerises partially and forms semi-solid parts of the structure at random locations within the metamaterial. This not only increases the overall mass of the experimental samples, but also negatively affects the mechanical performance by altering the internal geometry of the structure and causing stress concentration points. To reduce the effects of this problem, the washing procedure was adjusted for each sample type ensuring that the volume of excess resin was minimised.

As can be seen in Figure 5 where representative shear samples from each of the types of 3D projected 4-polytopes are shown; gyroid and honeycomb specimens were also manufactured for the purpose of comparison. The gyroid structure was chosen since there is a common research interest in the mechanical properties of this structure [54, 55] and the hexagonal honeycomb geometry was used for comparison, since it is used ubiquitously in industrial materials such as lightweight sandwich panels [56, 57]. The geometrical parameters of the gyroid shape had a sinusoidal wave amplitude of 2.5mm and a period of 20 mm with a wall thickness of 0.5mm. The structure had an apparent density of 143.44 kg/m^3 and a relative density of 12.32%. The honeycomb sample was made from hexagonal cells that closely mimic industrially available honeycomb core (CEL Components - PP8.120T30) [58] with a cell diameter of 8mm

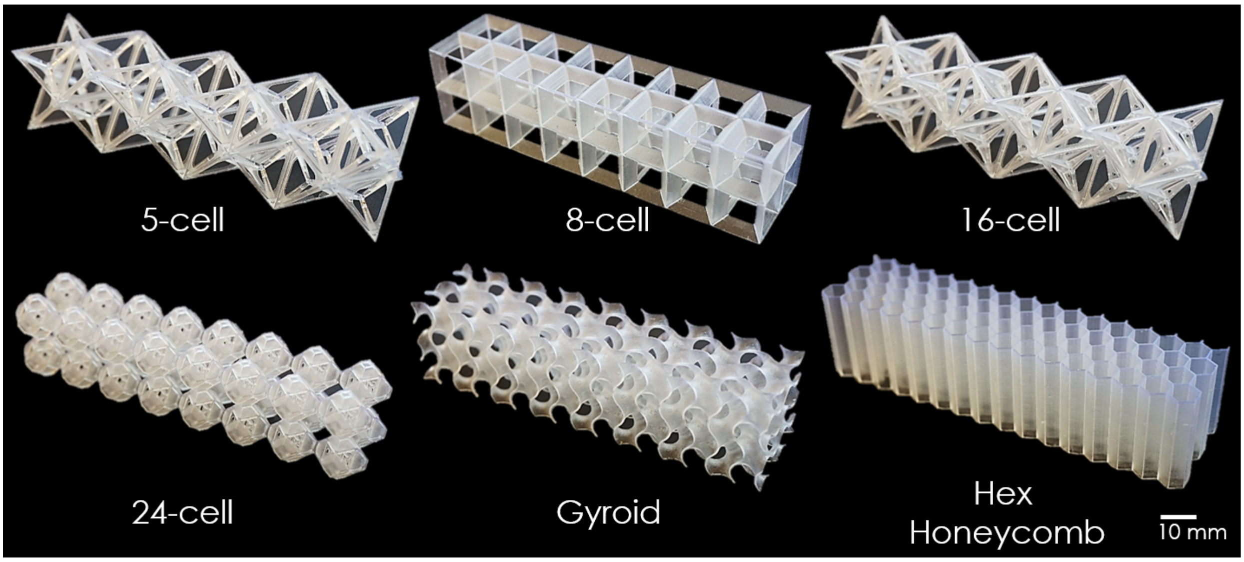

Figure 5: Representative shear test specimens with a $2 \times 2 \times 8$ 3D projected 4-polytope unit cell array. From left to right, 5-cell, 8-cell, 16-cell and 24-cell, and additional structures used as 'comparative experimental controls' - gyroid and hexagonal honeycomb.

and a wall thickness of 0.55mm, while the apparent and the relative densities for the sample were found to be 179.07 kg/m^3 and 15.38% respectively.

2.5. *Mechanical testing procedure*

Samples shown in Figure 5 (a total of 5 for each sample series) were mechanically tested using an Instron 3369 mechanical test machine using a load cell of 50kN. 3-point bend tests were conducted using an effective span-to-depth ratio of 2 to ensure that the specimens were loaded in shear [30]. Surface strains were measured with a 2D digital image correlation equipment (Imetrum DIC system with 1400×1000 resolution at 17.8fps). The strain measurements were taken to track the deflection in the middle of the sample caused by the downward crosshead movement with respect to the stationary support pins located at the bottom of the sample. Five specimens were tested for each of the four 4-polytope projections, as well as for the gyroid and honeycomb (out-of-plane orientation) structures, each using identical test set-ups. A ramp loading rate of 10mm/min was used to ensure Hookean behaviour of the bulk material under shear loading.

3. Results and Discussion

3.1. *Simulation results*

The 4-polytope projected metamaterial structures in shear were developed using the optimisation framework discussed in Section 2.3. The objective function focussed on maximising specific shear stiffness. The unit cell designs were generated in an iterative manner and their performance was evaluated and ranked according to the objective function. Figure 6 shows the results of incremental performance advancements for each 3D projected 4-polytope unit cell in shear. The stacked column chart shows the specific stiffness values of these metamaterial unit cells evaluated at several progression levels during the optimisation process, namely at 0% (unoptimised), 25%, 50%, 75% and 100% (fully optimised) of total optimisation.

The incremental specific shear stiffness improvements shown here, represent design space exploration that was carried out by the optimisation algorithm with higher performance enhancements during the intermediate iterations (optimisation levels 25%-75%) and smaller improvements as the near-optimum solution (fully optimised) is approached. The specific stiffness improvements between the unoptimised and fully optimised structures were found to be 4151.53%, 1279.84%, 275.15% and 281.63% for 5, 8, 16 and 24-cell structures respectively. The percentage

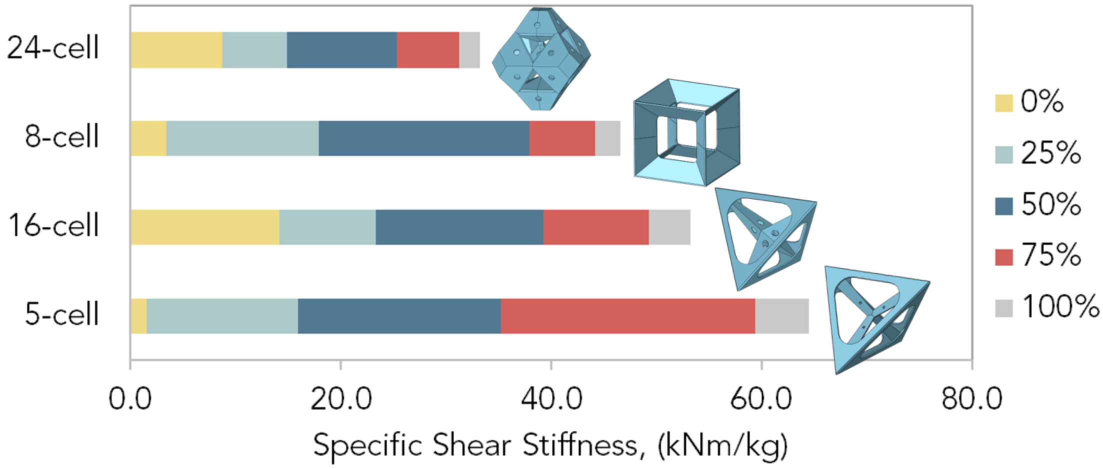

Figure 6: Specific shear stiffness comparison for the 5, 8, 16 and 24-cell polytopes in shear as the optimisation advances from unoptimised (0%) to fully-optimised (100%) state in 25% progression increments.

improvement values are highly dependent on the performance of the initial (unoptimised) structure which was designed without any insight from computer simulations, nevertheless, the results demonstrate the capabilities and the significance of using a simulation-based approach to optimising the structures. The lowest performance improvement was observed in the 24-cell unit cell, which was 2.75 times higher than that of its original design. The structure with the overall best specific shear stiffness properties was found to be the 5-cell structure with a value of 64.46 kNm/kg at the end of the optimisation cycle. It is also the design that benefited the most from the optimisation framework out of the four metamaterial unit cells analysed.

Figure 7 illustrates the total elastic strain energy density distribution (ESEDEN) resulting from shear loading, for each of the 4-polytope projected unit cells at the following optimisation levels: 0% (unoptimised), 25%, 50%, 75% and 100% (fully optimised). The colour distributions in each unit cell indicate geometrical regions that contribute the most towards load bearing under shear, and which are most involved in elastic strain energy storage. The strain energy density is noticeably more evenly distributed within the solid continuum of a structure as the optimisation progresses from 0-100%. As a result, more geometrically optimised structures have an increased overall capacity to store elastic strain energy resulting from loading in shear, which is in turn related to the overall stiffness of the unit cell. Consequently, when the apparent density of the unit cells is factored in, the fully optimised unit cells have the highest specific shear stiffness values as previously illustrated in Figure 6.

Due to the direction and the nature of the applied shear loading (discussed in Section 2.2), it can also be seen that the geometrical features at the corners of each unit cell are the regions with higher strain energy densities and these regions hence have a significant contribution towards the overall stiffness of the metamaterial structure, as visible in the right column of Figure 6 where fully optimised unit cell structures are shown. This is particularly evident in 5-cell and 16-cell structures, which also benefit from the geometrical features within the unit cells, which acting as cross-bracing, joining and stabilising the corners of the unit cell. The geometrical features inside the unit cells help share the load more effectively and provide additional stiffness to the structure. These are critical factors in 5-cell and 16-cell structures, which exhibit the highest specific shear properties. Between the two mentioned structures, the strain energy can be seen to be more evenly distributed within the 5-cell, while the 16-cell has a comparatively higher strain energy density concentration at the unit cell corners but lower strain energy density values within the internal cross-bracing structure, resulting in a lower overall capacity for strain energy storage. The 8-cell structure has a comparatively more even distribution of strain energy density within the structure, however, its geometry does not contain any cross-bracing geometrical features within the unit cell and as a consequence, 8-cell structures have a lower specific shear stiffness than the 5-cell and the 16-cell. The 24-cell structure has strain energy concentrated to some of the outer edges and also some inner geometrical regions that do not contribute to the overall strain energy storage capacity. This is partially due to the 24-cell having higher levels of geometrical complexity in comparison to

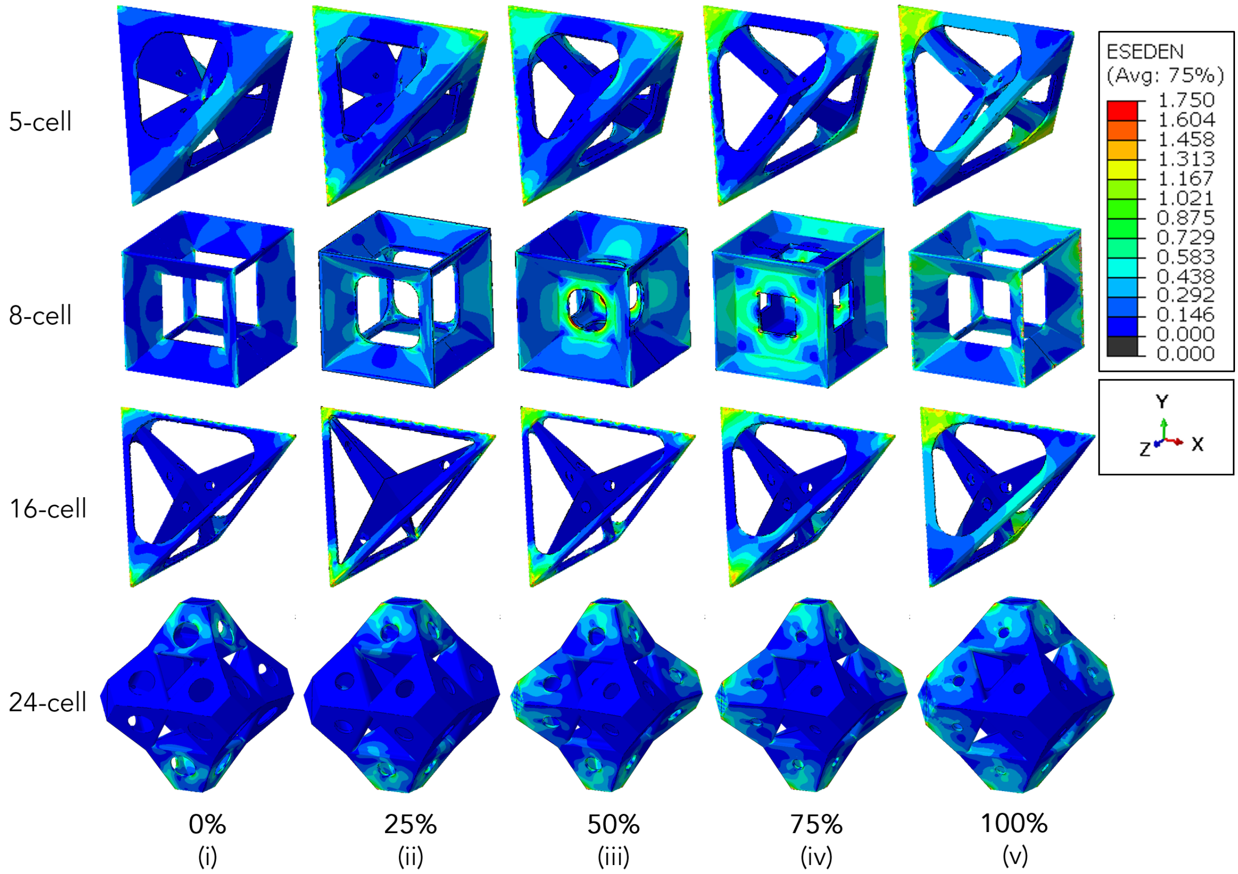

Figure 7: Colour maps for each of the 4-polytopes with each column illustrating optimisation progression at a different level: (i) 0% (unoptimised), (ii) 25%, (iii) 50%, (iv) 75% and (v) 100% of total optimisation (fully-optimised) metamaterial unit cells. The colour legend represents a range of elastic strain energy density (ESEDEN) values in J/cm^3 when the cells are loaded in shear to 0.10 strain.

other projected 4-polytope metamaterials resulting in more slender edges and sharper corner features within the unit cell. Such an uneven arrangement results in the lowest specific shear stiffness values out of the four unit cell structures discussed here.

3.2. *Experimental testing results*

Experimentally obtained specific shear stiffness and specific shear yield strength values are shown in Figure 8 for the 3D projected 4-polytope structures. The arithmetic mean values of each specific property are shown based on five specimens ($n = 5$) in each sample set, and the vertical and horizontal error bars represent the total range of experimental values obtained for each property. For comparison purposes, the data for cubically symmetrical gyroid structures and hexagonal honeycomb structure tested in shear in an out-of-plane direction are also included in the plot. Both of these structures were manufactured in the same manner as the 3D projected 4-polytope metamaterials, with the further details in Section 2.4.

The experimental specific shear stiffness results shown in Figure 8 closely follow the simulation predictions (Figure 6) with the 5-cell geometry having the highest specific stiffness value of 57.55 kNm/kg and a percentage difference of 10.71% when compared to the simulation output. In descending order, the mean experimental specific shear stiffness values are 52.73, 43.52, 29.58 kNm/kg for the 16-cell, 8-cell and 24-cell structures, respectively. The difference between the simulation and experimental results were found to be 6.54%, 0.97% and 10.93% for 16-cell, 8-cell and 24-cell structures, respectively. As previously shown by the modelling results (Section 3.1), the metamaterial structures with 1) geometrical features acting as stiffeners at the corner of each unit cell and 2) cross-bracing geometries joining the opposite corners of a unit cell contribute significantly towards increasing the shear resistance. This is evident in 5-cell and 16-cell geometries which outperform the remaining structures investigated, when comparing both experimental and simulation results. The specific shear stiffness results are comparatively lower for the metamaterials with geometrical features that are less in line with the shear forces, namely 8-cell and 24-cell structures. This corroborates the simulation results summarised in Figure 7 and demonstrates that the unit cell geometries with less evenly distributed strain energy densities tend to have a reduced capacity for strain energy storage, and therefore also have lower specific stiffness values.

The experimental results of gyroid and hexagonal honeycomb structures are also compared in Figure 8. Similarly to 8 and 24-cell unit cells, these structures do not possess geometrical features that could act as cross-bracing or corner-stiffening elements and therefore the specific shear stiffness values are low, being 30.02 and 22.82 kNm/kg for gyroid and honeycomb, respectively. When compared to the best-performing 4-polytope-based structure, the 5-cell specific shear stiffness surpasses that of the gyroid and hexagonal honeycomb structures by 1.9 and 2.5 times, respectively.

In addition to high specific shear stiffness values, all of the metamaterials based on 3D projected 4-polytopes, namely 5, 8, 16 and 24-cell, also outperform the gyroid and hexagonal honeycomb structures in terms of specific shear yield strength. As shown in Figure 8, 8-cell has the highest specific shear yield strength, followed by the 5-cell, 16-cell and 24-cell geometries with the values of 2.03, 1.66, 1.18 and 0.98 kNm/kg respectively. The yield strength values for the gyroid and hexagonal honeycomb were found to be 0.46 and 0.84 kNm/kg respectively. The experimental values obtained for the 8-cell, the best-performing structure in terms of the specific shear yield strength, are 4.41 and 2.41 times higher than those of the gyroid and hexagonal honeycomb structures respectively. These results indicate that although the 8-cell has lower specific shear stiffness than the 5 and 16-cell structures, its cubical geometry with thin walls aligned along the diagonal directions of a unit cell offers great strength when loaded in shear. The lack of cross-bracing elements in the unit cell geometry affects the overall stiffness of the structure, however, the interconnected thin walls and a well-balanced selection of feature sizes minimising internal stress concentrations are the two factors most plausibly contributing towards the high specific shear yield strength of the unit cell.

All of the 3D projected 4-polytope metamaterials developed and analysed in this work, benefit from the cubically symmetrical unit cells, which have identical mechanical properties along their three orthogonal axes. This is unlike the honeycomb structures which show superior out-of-plane than in-plane mechanical stiffness and strength [51]. The results presented here demonstrate that 4-polytope projected metamaterials can not only outperform commercially available honeycomb structures, but also outperform other commonly researched metamaterials with cubically symmetric unit cells, such as gyroid structures.

The simulation and experimental results discussed in the preceding paragraphs are also presented in Tables 3 and 4, summarising specific shear stiffness and specific shear yield strength results respectively. Statistical details such as experimental range, median, standard deviation and the coefficient of variance (CoV) are included for the experimental results. The tables also present a comparison between experimental and simulation results with the percentage difference values quoted for each sample set, and a Z-score (Z) value calculated as $Z = \frac{\frac{G}{\rho} - \frac{\bar{G}}{\rho}}{S}$ for the specific shear stiffness case and as $Z = \frac{\frac{\tau_y}{\rho} - \frac{\bar{\tau}_y}{\rho}}{S}$ for the specific shear yield strength case, where S is the standard deviation of each sample set.

As shown in Table 3, the simulation results for specific shear stiffness are 0.97%, 6.54%, 10.71% and 10.93% higher than the experimentally obtained values for the 16, 8, 5 and 24-cell structures. Similar tendencies between the simulation outputs and experimental results are demonstrated by the low Z-score values which are in the range of 0.03 to 1.22 for the specific shear stiffness results. While the modelling outputs tend to overestimate performance of the metamaterials, these results also indicate that the simulation accuracy for predicting the specific shear stiffness values are high, and the simulation and experimental results are in good agreement. The specific shear stiffness values are most accurately predicted for the 16-cell structure.

However, a different trend is evident when analysing specific shear yield strength results summarised in Table 4. The percentage difference values comparing simulation against experimention are in the range of 10.85% and 36.34%, with the most accurate prediction of the 5-cell performance and the least accurate outputs for the 24-cell. The Z-scores also indicate higher levels of discrepancy with values of 1.30, 1.95, 2.79 and 4.89 in increasing order for the 5, 16, 24 and 8-cell, respectively.

The results are also visualised in Figure 9 with the simulation-predicted shear stress - shear strain curves plotted

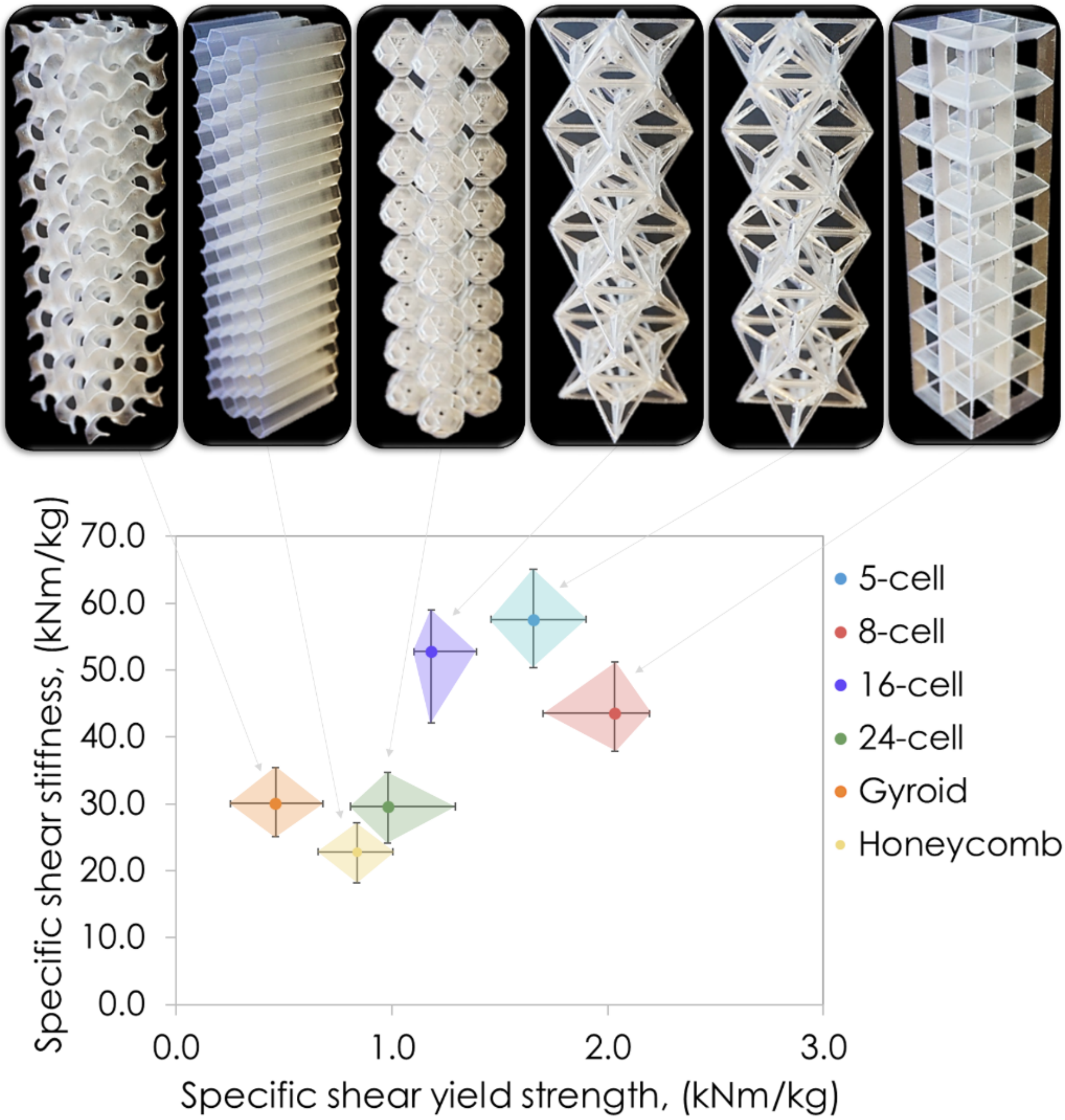

Figure 8: Specific shear properties plot for experimental 4-polytope-based metamaterial samples together with gyroid and honeycomb structures.

in dashed lines and the upper and lower experimental testing bounds plotted with solid lines. The specific shear stiffness show high predictive accuracy, especially at low strains, while the simulation results closely follow the upper experimental curves for each of the 3D projected 4-polytope metamaterials. This trend is especially evident at the low shear strains where the shear stress - shear strain curves start diverging, and the experimental samples reach an onset of plasticity at lower shear strain values than as predicted by modelling. As a result, the 4-polytope projected metamaterials enter the plastic deformation stage earlier, and the experimental specific shear yield strengths are lower than as predicted by the simulations.

The main reasons for the differences between the simulated and experimentally obtained specific shear yield strength values are 1) manufacturing limitations, 2) shear test limitations and 3) a low number of neighbouring unit cells in the shear specimens. Firstly, the manufacturing limitations stem from the limitations of SLA 3D printing

Table 3: Mean specific shear stiffness $\left(\frac{\bar{G}}{\rho}\right)$ results for experimental samples: 5, 8, 16 and 24-cell metamaterials, as well as gyroid and honeycomb structures and specific shear stiffness values $\left(\frac{G}{\rho}\right)$ for simulated models: 5, 8, 16 and 24-cell metamaterials.

Experimental	5-cell	8-cell	16-cell	24-cell	Gyroid	Hex honeycomb
Mean shear specific stiffness $\left(\frac{\bar{G}}{\rho}\right)$, (kNm/kg)	57.55	43.52	52.73	29.58	30.02	22.82
Upper value	65.05	51.24	63.32	34.71	32.15	27.13
Lower value	50.40	37.81	17.60	20.98	26.56	18.11
Median	56.78	41.40	46.54	25.58	30.02	23.13
Standard deviation	5.66	5.36	16.07	5.50	2.14	2.86
CoV	9.83%	12.32%	30.47%	18.59%	7.13%	12.55%
Simulation						
Specific shear stiffness $\left(\frac{G}{\rho}\right)$, (kNm/kg)	64.46	46.56	53.25	33.21	N/A	N/A
Percentage diff. (sim. vs exp.)	10.71%	6.54%	0.97%	10.93%	N/A	N/A
Z-score	1.22	0.57	0.03	0.66	N/A	N/A

Table 4: Mean specific shear yield strength $\left(\frac{\bar{\tau}_y}{\rho}\right)$ results for experimental samples: 5, 8, 16 and 24-cell metamaterials, as well as gyroid and honeycomb structures, and specific shear strength values $\left(\frac{\tau_y}{\rho}\right)$ for simulated models: 5, 8, 16 and 24-cell metamaterials.

Experimental	5-cell	8-cell	16-cell	24-cell	Gyroid	Hex honeycomb
Mean specific shear yield strength $\left(\frac{\bar{\tau}_y}{\rho}\right)$, (kNm/kg)	1.66	2.03	1.18	0.98	0.46	0.84
Upper value	1.90	2.19	1.88	1.29	0.52	1.00
Lower value	1.46	1.70	1.10	0.70	0.41	0.66
Median	1.67	2.13	1.12	0.87	0.46	0.83
Standard deviation	0.15	0.18	0.30	0.20	0.04	0.11
CoV	9.34%	8.73%	25.41%	20.47%	8.72%	13.44%
Simulation						
Specific shear yield strength $\left(\frac{\tau_y}{\rho}\right)$, (kNm/kg)	1.86	2.90	1.77	1.54	N/A	N/A
Percentage diff. (sim. vs exp.)	10.85%	29.90%	33.18%	36.34%	N/A	N/A
Z-score	1.30	4.89	1.95	2.79	N/A	N/A

methodology, and our aim to manufacture geometrically complex structures. As discussed in Section 2.4, the 3D projected 4-polytope metamaterials contain geometrical pockets where resin can accumulate, and this is not fully removed when the samples are post-processed. The leftover resin then solidifies during the post-curing process and creates stress concentration points, leading to an early onset of plasticity. This also results in a higher sample weight, which in turn negatively affects the specific properties of experimentally tested metamaterials. Secondly, the limitations of a 2D DIC system used for measuring the surface strains in a 3-point bend test contribute to potential inaccuracies in the experimental results. The 2D system neither captures the out-of-plane nor the internal unit cell deformations and therefore contributes to measurement-related inaccuracies. Thirdly, the maximum size of the specimens is limited by the build volume of the 3D printer, the samples have a low number of neighbouring unit cells and therefore suffer from boundary effects which are not accounted for in the simulations. The 2×2 arrangement of the unit cells in a cross-section of a specimen is considered as low as for a unit-cell-based structure. Computational modelling work published by [59] suggests that the specimen cross-section to unit size ratio should exceed 10 to appropriately homogenise the mechanical metamaterial. It should also be noted that the modelling work presented here does not account for any manufacturing-related imperfections, assumes periodic boundary conditions, and hence idealises the metamaterial performance. Therefore, at low shear strains when the stress levels within the material are low and material imperfections are not the key factors affecting the metamaterial response and therefore the specific shear stiffness predictions are of high accuracy.

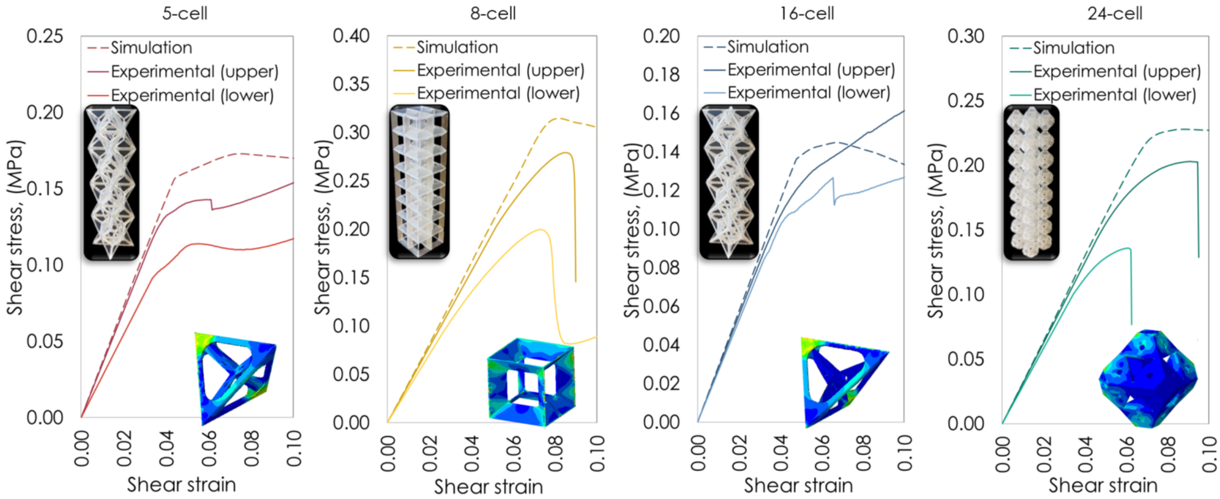

Figure 9: Shear stress-strain curves for 5, 8, 16 and 24-cell meta-structures. Upper and lower experimental bounds are presented in solid lines while simulated results are shown as dashed lines.

The mechanical metamaterial properties discussed up until now were highly influenced by the computational methods, which were aimed at maximising the metamaterial elastic strain energy capacity under shear. This enabled the enhancement of specific shear stiffness and specific shear yield strength properties of the 4-polytope projected metamaterials. However, to better understand the effect of the computational optimisation approach on basic mechanical properties (excluding the effect of lightweightness), and hence the general mechanical behaviour of these structures, Table 5 summarises shear modulus, shear yield and shear strength as well as modulus of resilience and toughness properties to evaluate metamaterial performance in a more generic sense. The values are presented for all of the 3D projected 4-polytope metamaterials, gyroid and hexagonal honeycomb structures. The summary also includes statistical details for standard deviation (SD) and coefficient of variance (CoV). The gyroid structure exhibits the highest shear stiffness with a modulus value of 4.31 MPa, closely followed by hexagonal honeycomb and 8-cell metamaterial structures which have a modulus value of 4.09 and 4.00 MPa respectively. The shear stiffness values for 5, 16 and 24-cell are 3.58, 2.69 and 2.95 MPa respectively. The coefficient of variance was found to be between 9.52% and 29.58% with standard deviation values between 0.35 and 0.80. A different trend is noticed when comparing the shear yield strength properties with the 8-cell structure having the highest value of 0.19 MPa which is 23.53% higher than that of a hexagonal honeycomb, which is the second best-performing structure. The rest of the 3D projected 4-polytopes, namely the 5, 16 and 24-cell outperform the gyroid by 35.29%, 13.33% and 35.21% respectively, which has the lowest stiffness among the compared metamaterials of 0.07 MPa. In terms of shear strength, the hexagonal honeycomb performs the best followed by the gyroid and the 8-cell with shear strength values of 0.37, 0.27 and 0.26 MPa respectively while the 5, 16 and 24-cell structures have the shear strength of 0.15, 0.16 and 0.17 MPa respectively. The modulus of resilience results follow a similar trend as summarised for the shear yield strength with the

Table 5: Summary of experimentally obtained mechanical properties: shear modulus, shear yield strength and shear strength, modulus of resilience and modulus of toughness for 4-polytope projected metamaterials, and for gyroid and hexagonal honeycomb structures.

	5-cell	8-cell	16-cell	24-cell	Gyroid	Hex honeycomb
Shear mod., (MPa)	3.58	4.00	2.69	2.95	4.31	4.09
SD	0.35	0.49	0.80	0.58	0.41	0.51
CoV	9.83%	12.32%	29.58%	19.74%	9.52%	12.55%
Shear yield strength, (MPa)	0.10	0.19	0.08	0.10	0.07	0.15
SD	0.01	0.02	0.02	0.02	0.02	0.02
CoV	9.34%	8.38%	22.72%	21.69%	29.52%	13.44%
Shear strength, (MPa)	0.15	0.26	0.16	0.17	0.27	0.37
SD	0.02	0.03	0.03	0.03	0.05	0.10
CoV	14.14%	11.42%	22.42%	18.59%	16.62%	26.12%
Mod. of resilience, (kJ/m^3)	1754	4197	918	2260	649	2502
SD	164	606	179	373	126	335
CoV	9.34%	14.45%	19.54%	16.49%	19.47%	13.39%
Mod. of toughness, (kJ/m^3)	24406	16840	15471	7215	34200	22965
SD	13318	4826	9110	2742	15470	8990
CoV	54.57%	28.66%	58.89%	38.00%	45.23%	39.14%

8-cell showing the maximum capacity for absorbing energy before the onset of plasticity, outperforming both the gyroid and the honeycomb structures by 146.43% and 50.60% respectively. The remaining 3D projected 4-polytope metamaterials outperform the gyroid structure. The metamaterials with the highest modulus of toughness values, in descending order, are the gyroid, 5-cell and honeycomb with the modulus of toughness of 34200, 24406 and 22965 kJ/m^3 respectively. This is followed by the 8-cell, 16-cell and 24-cell structures with respective modulus of toughness values of 16840, 15471 and 7215 kJ/m^3. Among the 3D projected 4-polytope metamaterials, the ones with the cross-bracing structural features, namely the 5 and 16-cell structures, tend to have a longer plastic region in comparison to 8 and 24-cell structures that lack the geometrical features joining the opposite corners of a unit cell together. The high modulus of toughness in 5-cell and 16-cell structures is mainly the result of the ability to sustain high shear strains prior to the occurrence of catastrophic failure with 5-cell and 16-cell failing at the shear strains of 0.13 and 0.10 respectively. This demonstrates the ability of the structures to absorb shear deformation energy through gradual plastic yielding, however, it is unclear how this behaviour occurring in only two of the four investigated 4-polytope-based structures is affected by the parametric optimisation aimed at maximising elastic strain energy storage.

Table 6: Apparent and relative densities for simulated and experimentally tested shear samples.

	Simulations		Experimental	
	Apparent density, (kg/m3)	Relative density	Apparent density, (kg/m3)	Relative density
5-cell	56.44	4.85%	62.13	5.34%
8-cell	86.71	7.45%	91.94	7.90%
16-cell	53.86	4.63%	58.89	5.06%
24-cell	96.25	8.27%	105.93	9.10%
Gyroid	N/A	N/A	143.44	12.32%
Honeycomb	N/A	N/A	179.07	15.38%

The results presented here provide a good indication of general metamaterial performance, however, they do not take the mass of each specimen into account. Table 6 summarises the apparent and relative densities of the simulated and experimentally tested structures compared in this publication. It is worth noting that the gyroid and hexagonal honeycomb structures which have the highest shear stiffness and strength properties also have the highest apparent density values. When compared to the 3D projected 4-polytope metamaterials, the apparent densities of gyroid and honeycomb specimens are 79.11% and 96.97% higher than the 5-cell and 43.75% and 64.30% higher than the 8-cell, which has the highest apparent density out of the three best-performing 4-polytope projected metamaterials. This emphasises the importance of comparing metamaterial structures using specific properties when ranking their performance.

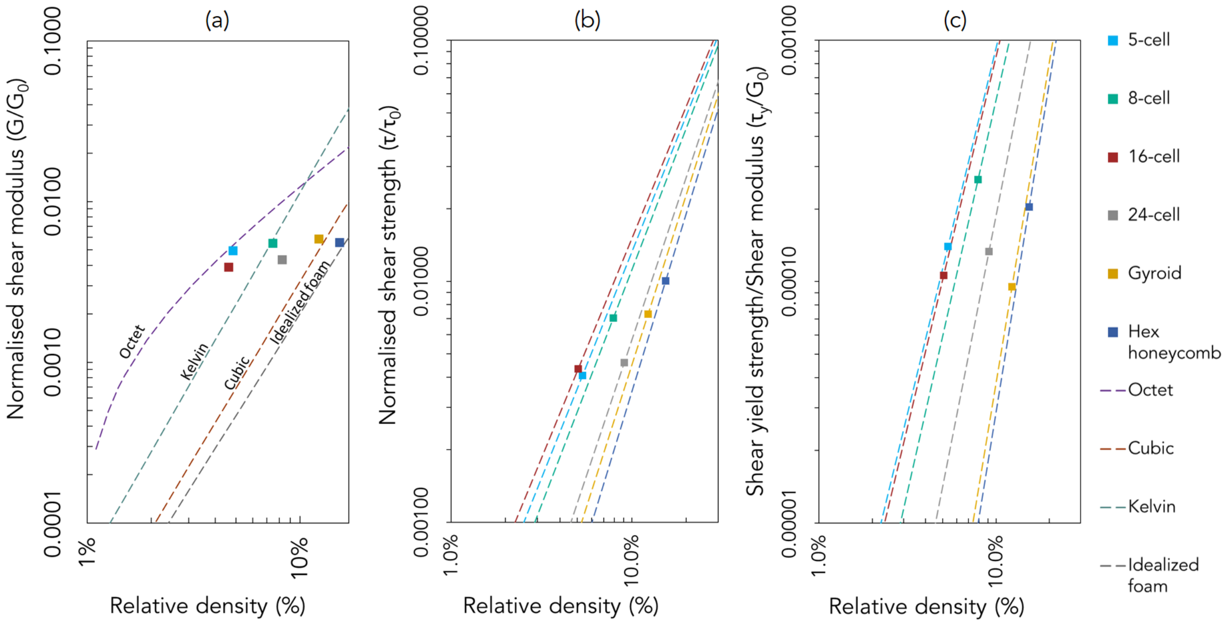

Figure 10: Experimental comparison of 4-polytope-based metamaterials with gyroid, hexagonal honeycomb samples, as well as other metamaterial structures presented in, [26, 31], namely, Kelvin, octet, idealized foam and cubic lattices. The figure presents the results for (a) normalised shear modulus (G/G_0), (b) normalised shear strength (τ/τ_0) and (c) shear yield strength over shear modulus (τ_y/G_0) plotted against the relative density. Parts (b) and (c) of the figure also include scaling law trendlines for all 4-polytope-based metamaterial structures and gyroid and hexagonal honeycomb samples.

An alternative way of comparing the structural performance of the metamaterials is presented in Figure 10. Here, the experimental results of 4-polytope projected metamaterials as well as gyroid and hexagonal honeycomb samples are compared using performance indices plotted against the relative density of each experimental sample. This normalisation method allows for the examining of stiffness and strength gained from the metamaterial structure, rather than from the bulk material properties [60]. Figure 10 (a) presents normalised shear modulus (G/G_0) with additional data included for metamaterial structures in, [26, 31], namely, Kelvin, octet, idealised foam and cubic lattices. It is evident that all 4-polytope projected metamaterials outperform idealised foam and cubic lattice structures in terms of their normalised shear modulus at a given relative density. The 5-cell and 16-cell structures also perform better when compared to the Kelvin lattice structure, while only the 5-cell structure has a similar normalised shear modulus to the octet truss.

In terms of normalised shear strength (Figure 10 (b)), 16-cell surpasses the rest of the 4-polytope metamaterials and is closely followed by the 5-cell structure both of which have similar geometrical cross-bracing features as discussed in Section 3.1. In the descending performance order, these two metamaterial structures are followed by the 8-cell, 24-cell, gyroid and hexagonal honeycomb structures.

The plot in 10 (c), shows the shear yield strength normalised by the shear modulus of the fully cured constituent material while this is presented against the relative density of each structure (also shown in Table 6). The figure shows that the 5-cell structure has the highest shear yield strength to shear modulus ratio with the lowest relative density indicating that this geometrical arrangement is the most suitable for applications requiring a high strength-to-weight ratio. The second best-performing geometrical arrangement is the 16-cell structure followed by the 8-cell, 24-cell, gyroid and hexagonal honeycomb structures. The figure also presents the relative density of the aforementioned structures with the 16-cell having the lowest value of 5.06% and the honeycomb having the highest of 15.38%. While

Figure 10 (c) compares the shear yield strength performance of the structures, it can also be used as a visualisation tool in future work allowing engineers to choose metamaterials most suited for the design application while taking the performance and apparent density into account.

Parts (b) and (c) of Figure 10 also include scaling law trendlines for the experimental results of 4-polytope projected metamaterial structures, gyroid and hexagonal honeycomb structures, adapting the same methodology as presented in [61]. The scaling law for the normalised shear strength is calculated as $\frac{\tau}{\tau_0} = (\frac{\rho}{\rho_0})^n$, where τ is the shear strength of a specimen, τ_0 and ρ_0 are shear strength and density of the constituent material respectively, ρ is the density of the specimen, and n is a positive integer found empirically for each individual structure. Similarly, the scaling law trendlines plotted in Figure 10 (c) were computed using $\frac{\tau_y}{G_0} = (\frac{\rho}{\rho_0})^m$, where τ_y is the shear yield strength of a specimen, G_0 is the shear modulus of the constituent material and m is a positive integer presenting the empirical value found for each metamaterial geometry. In the case of normalised shear strength (b) the scaling law n values are 1.88, 1.95, 1.82, 2.24, 2.35, 2.46 and in the case of shear yield strength over constituent material shear modulus (c), the values for m were found to be 3.03, 3.25, 3.07, 3.72, 4.42, 4.54 for 5-cell, 8-cell, 16-cell, 24-cell, gyroid and hexagonal honeycomb structures, respectively.

4. Conclusions

This article discusses a new class of mechanical metamaterials based on 4^{th} dimensional shadows projected into 3-space and optimised for shear resistance. The methodology presented here demonstrates that the performance of these structures can not only be tailored to a specific application but also enhanced more than 40 times in terms of specific shear properties by employing an evolutionary algorithm-powered optimisation framework. The results suggests that the cubically symmetrical 4-polytope projected metamaterials outperform other commonly researched structures such as gyroid and hexagonal honeycombs in terms of both specific shear stiffness and specific shear yield strength. Among the structures examined here, the 5-cell (pentatope) demonstrates a shear stiffness that is nearly double that of a gyroid structure. This superior performance is attributed to the presence of cross-bracing within the 5-cell, which is also present in the second-best-performing 16-cell structure. The 8-cell (tesseract) shows the highest specific shear yield strength, surpassing the hexagonal honeycomb tested in the out-of-plane direction by 2.4 times, and hence offering the advantages where a high strength-to-weight ratio is required. The 24-cell structure demonstrates the lowest values for both specific shear stiffness and shear yield strength out of the four investigated 4-polytope projected structures, while having almost the same specific shear stiffness as the gyroid and higher specific shear yield strength than the hexagonal honeycomb. The normalised shear modulus results are also benchmarked against a range of metamaterial structures investigated in the available literature, showing the potential of 3D projected 4-polytope metamaterials. The cubically symmetrical 4-polytope projected designs, lightweightness and high shear resistance provide significant benefits in maintaining structural stiffness when subjected to multi-axial loading, which is advantageous in many real-life applications.

Author Contributions

Conceptualisation (PA); Data curation (GC and PA); Formal analysis (GC and PA); Funding acquisition (GC and PA); Investigation (GC); Methodology (GC and PA); Project administration (GC and PA); Resources (GC and PA); Software (GC); Supervision (PA); Validation (GC and PA); Visualisation (GC and PA); Roles/Writing - original draft (GC); Writing - review and editing (PA).

References

[1] J. U. Surjadi, L. Gao, H. Du, X. Li, X. Xiong, N. X. Fang, Y. Lu, Mechanical Metamaterials and Their Engineering Applications, Advanced Engineering Materials 21 (3) (2019) 1–37. doi:10.1002/adem.201800864.

[2] M. Kadic, G. W. Milton, M. Van Hecke, M. Wegener, 3D metamaterialsdoi:10.1038/s42254-018-0018-y.
URL www.nature.com/natrevphys

[3] E. Truszkiewicz, A. Thalhamer, M. Rossegger, M. Vetter, G. Meier, E. Rossegger, P. Fuchs, S. Schlögl, M. Berer, Mechanical behavior of 3D-printed polymeric metamaterials for lightweight applications, Journal of Applied Polymer Science 139 (6) (2 2022). doi:10.1002/APP.51618.

[4] W. Lv, D. Li, L. Dong, Study on mechanical properties of a hierarchical octet-truss structure, Composite Structures 249 (2020) 112640. doi:10.1016/J.COMPSTRUCT.2020.112640.

[5] X. Zheng, H. Lee, T. H. Weisgraber, M. Shusteff, J. DeOtte, E. B. Duoss, J. D. Kuntz, M. M. Biener, Q. Ge, J. A. Jackson, S. O. Kucheyev, N. X. Fang, C. M. Spadaccini, Ultralight, ultrastiff mechanical metamaterials, Science 344 (6190) (2014) 1373–1377. doi:10.1126/SCIENCE.1252291/SUPPL{_}FILE/ZHENG.SM.PDF.
URL https://www.science.org/doi/10.1126/science.1252291

[6] M. Fleisch, A. Thalhamer, G. Meier, I. Raguž, P. F. Fuchs, G. Pinter, S. Schlögl, M. Berer, Functional mechanical metamaterial with independently tunable stiffness in the three spatial directions, Materials Today Advances 11 (9 2021). doi:10.1016/J.MTADV.2021.100155.

[7] M. Taghavi, T. Helps, B. Huang, J. Rossiter, 3D-Printed Ready-To-Use Variable-Stiffness Structures, IEEE Robotics and Automation Letters 3 (3) (2018) 2402–2407. doi:10.1109/LRA.2018.2812917.

[8] I. Cazin, M. O. Gleirscher, M. Fleisch, M. Berer, M. Sangermano, S. Schlögl, Spatially controlling the mechanical properties of 3D printed objects by dual-wavelength vat photopolymerization, Additive Manufacturing 57 (9 2022). doi:10.1016/J.ADDMA.2022.102977.

[9] X. Ren, Y. Zhang, C. Z. Han, D. Han, X. Y. Zhang, X. G. Zhang, Y. M. Xie, Mechanical properties of foam-filled auxetic circular tubes: Experimental and numerical study, Thin-Walled Structures 170 (1 2022). doi:10.1016/J.TWS.2021.108584.

[10] D. Han, X. Ren, C. Luo, Y. Zhang, X. Y. Zhang, X. G. Zhang, W. Jiang, J. Hao, Y. M. Xie, Experimental and computational investigations of novel 3D printed square tubular lattice metamaterials with negative Poisson's ratio, Additive Manufacturing 55 (7 2022). doi:10.1016/J.ADDMA.2022.102789.

[11] X. Zheng, T. T. Chen, X. Guo, S. Samitsu, I. Watanabe, Controllable inverse design of auxetic metamaterials using deep learning, Materials & Design 211 (2021) 110178. doi:10.1016/J.MATDES.2021.110178.

[12] A. A. Zadpoor, Mechanical meta-materials, Mater. Horiz. 3 (2016) 371–381. doi:10.1039/C6MH00065G.
URL http://dx.doi.org/10.1039/C6MH00065G

[13] Z. Li, Z. Luo, L.-C. Zhang, C.-H. Wang, Topological design of pentamode lattice metamaterials using a ground structure method, Materials and Design 202 (2021). doi:10.1016/j.matdes.2021.109523.

[14] S. Wu, Z. Luo, Z. Li, S. Liu, L. C. Zhang, Topological design of pentamode metamaterials with additive manufacturing, Computer Methods in Applied Mechanics and Engineering 377 (2021) 113708. doi:10.1016/J.CMA.2021.113708.

[15] Z. Zou, F. Xu, Y. Pan, X. Niu, T. Fang, C. Zeng, Parametric Analysis and Multi-Objective Optimization of Pentamode Metamaterial, Sustainability 2023, Vol. 15, Page 3421 15 (4) (2023) 3421. doi:10.3390/SU15043421.
URL https://www.mdpi.com/2071-1050/15/4/3421/htmhttps://www.mdpi.com/2071-1050/15/4/3421

[16] A. Amendola, C. J. Smith, R. Goodall, F. Auricchio, L. Feo, G. Benzoni, F. Fraternali, Experimental response of additively manufactured metallic pentamode materials confined between stiffening plates, Composite Structures 142 (2016) 254–262. doi:10.1016/J.COMPSTRUCT.2016.01.091.

[17] M. Fleisch, A. Thalhamer, G. Meier, P. A. F. Huber, P. F. Fuchs, G. Pinter, S. Schlögl, M. Berer, Chiral-based mechanical metamaterial with tunable normal-strain shear coupling effect, Engineering Structures 284 (2023) 115952. doi:10.1016/J.ENGSTRUCT.2023.115952.

[18] X. Li, Z. Yang, Z. Lu, Design 3D metamaterials with compression-induced-twisting characteristics using shearâcompression coupling effects, Extreme Mechanics Letters 29 (2019) 100471. doi:10.1016/J.EML.2019.100471.

[19] W. Wu, W. Hu, G. Qian, H. Liao, X. Xu, F. Berto, Mechanical design and multifunctional applications of chiral mechanical metamaterials: A review, Materials & Design 180 (2019) 107950. doi:10.1016/J.MATDES.2019.107950.

[20] N. Karathanasopoulos, F. Dos Reis, M. Diamantopoulou, J. F. Ganghoffer, Mechanics of beams made from chiral metamaterials: Tuning deflections through normal-shear strain couplings, Materials & Design 189 (2020) 108520. doi:10.1016/J.MATDES.2020.108520.

[21] S. Jin, Y. P. Korkolis, Y. Li, Shear resistance of an auxetic chiral mechanical metamaterial, International Journal of Solids and Structures 174-175 (2019) 28–37. doi:https://doi.org/10.1016/j.ijsolstr.2019.06.005.
URL https://www.sciencedirect.com/science/article/pii/S0020768319302835

[22] X. Tan, B. Wang, K. Yao, S. Zhu, S. Chen, P. Xu, L. Wang, Y. Sun, Novel multi-stable mechanical metamaterials for trapping energy through shear deformation, International Journal of Mechanical Sciences 164 (2019) 105168. doi:10.1016/J.IJMECSCI.2019.105168.

[23] H. Zhang, P. Chen, G. Lin, W. Sun, A corrugated gradient mechanical metamaterial: Lightweight, tunable auxeticity and enhanced specific energy absorption, Thin-Walled Structures 176 (2022) 109355. doi:10.1016/J.TWS.2022.109355.

[24] S. Liu, A. I. Azad, R. Burgueño, Architected materials for tailorable shear behavior with energy dissipation, Extreme Mechanics Letters 28 (2019) 1–7. doi:10.1016/J.EML.2019.01.010.

[25] C. Mei, L. Li, X. Li, Y. Jiang, X. Han, H. Tang, X. Wang, Y. Hu, Spatiotemporal damping of dissipative metamaterial, International Journal of Mechanical Sciences 254 (2023) 108393. doi:10.1016/J.IJMECSCI.2023.108393.
URL https://linkinghub.elsevier.com/retrieve/pii/S0020740323002953

[26] I. Arretche, K. H. Matlack, On the interrelationship between static and vibration mitigation properties of architected metastructures, Frontiers in Materials 5 (11 2018). doi:10.3389/FMATS.2018.00068.

[27] J. B. Berger, H. N. Wadley, R. M. McMeeking, Mechanical metamaterials at the theoretical limit of isotropic elastic stiffness, Nature 2016 543:7646 543 (7646) (2017) 533–537. doi:10.1038/nature21075.
URL https://www.nature.com/articles/nature21075

[28] S. Lee, Z. Zhang, G. X. Gu, Deep learning accelerated design of mechanically efficient architected materials, ACS Applied Materials & Interfaces 15 (18) (2023) 22543–22552, pMID: 37105969. doi:10.1021/acsami.3c02746.
URL https://doi.org/10.1021/acsami.3c02746

[29] Q. Liu, Y. Long, J. Ge, Y. Zhou, P. Huang, S. Yuan, Z. Zhang, T. Shi, A novel approach for mechanical regulation of thin-walled crystal plate lattices: Experimental characterization and simulation, Materials and Design 223 (11 2022). doi:10.1016/J.MATDES.2022.111122.

[30] A. C. Manalo, Behaviour of fibre composite sandwich structures under short and asymmetrical beam shear tests, Composite Structures 99 (2013) 339–349. doi:10.1016/j.compstruct.2012.12.010.
URL http://dx.doi.org/10.1016/j.compstruct.2012.12.010

[31] L. Shu, R. Liang, Y. Yu, T. Tian, Z. Rao, Y. Wang, Unique elastic, dielectric and piezoelectric properties of micro-architected metamaterials, Journal of Materials Chemistry C 7 (9) (2019) 2758–2765. doi:10.1039/C8TC05847D.
URL https://www.researchgate.net/publication/342589960_Unique_elastic_dielectric_and_piezoelectric_properties_of_micro-architected_metamaterials

[32] G. X. Gu, C.-T. Chen, M. J. Buehler, De novo composite design based on machine learning algorithm, Extreme Mechanics Letters 18 (2018) 19–28. doi:https://doi.org/10.1016/j.eml.2017.10.001.
URL https://www.sciencedirect.com/science/article/pii/S2352431617301256

[33] R.-B. Yang, J. Yang, S. Lo, Wideband square spiral metamaterial absorbers based on flaky carbonyl iron/epoxy composites, AIP Advances 10 (1) (2020). doi:10.1063/1.5130470.

[34] L. Singleton, J. Cheer, S. Daley, Design of a resonator-based metamaterial for broadband control of transverse cable vibration, in: Proceedings of the International Congress on Acoustics, Vol. 2019-September, International Commission for Acoustics (ICA), 2019, pp. 5589–5596. doi:10.18154/RWTH-CONV-239432.

[35] M. Mansouree, A. Arbabi, Metasurface Design Using Level-Set and Gradient Descent Optimization Techniques, in: 2019 International Applied Computational Electromagnetics Society Symposium in Miami, ACES-Miami 2019, Institute of Electrical and Electronics Engineers Inc., 2019.

[36] Y. Wang, Q. Zeng, J. Wang, Y. Li, D. Fang, Inverse design of shell-based mechanical metamaterial with customized loading curves based on machine learning and genetic algorithm, Computer Methods in Applied Mechanics and Engineering 401 (2022) 115571. doi:10.1016/J.CMA.2022.115571.

[37] L. Wang, H.-T. Liu, Parameter optimization of bidirectional re-entrant auxetic honeycomb metamaterial based on genetic algorithm, Composite Structures 267 (2021). doi:10.1016/j.compstruct.2021.113915.

[38] M. Bessa, P. Glowacki, M. Houlder, Bayesian Machine Learning in Metamaterial Design: Fragile Becomes Supercompressible, Advanced Materials 31 (48) (2019). doi:10.1002/adma.201904845.

[39] H. M. Sheikh, T. Meier, B. Blankenship, Z. Vangelatos, N. Zhao, P. S. Marcus, C. P. Grigoropoulos, Systematic design of Cauchy symmetric structures through Bayesian optimization, International Journal of Mechanical Sciences (2022) 107741doi:10.1016/J.IJMECSCI.2022.107741.

[40] Z. Vangelatos, H. M. Sheikh, P. S. Marcus, C. P. Grigoropoulos, V. Z. Lopez, G. Flamourakis, M. Farsari, Strength through defects: A novel Bayesian approach for the optimization of architected materials, Science Advances 7 (41) (10 2021). doi:10.1126/SCIADV.ABK2218/SUPPL{_}FILE/SCIADV.ABK2218{_}MOVIES{_}S1{_}TO{_}S4.ZIP.
URL https://www.science.org/doi/10.1126/sciadv.abk2218

[41] O. Khatib, S. Ren, J. Malof, W. J. Padilla, O. Khatib, S. Ren, J. Malof, W. J. Padilla, Deep Learning the Electromagnetic Properties of MetamaterialsâA Comprehensive Review, Advanced Functional Materials 31 (31) (2021) 2101748. doi:10.1002/ADFM.202101748.
URL https://onlinelibrary.wiley.com/doi/full/10.1002/adfm.202101748https://onlinelibrary.wiley.com/doi/abs/10.1002/adfm.202101748https://onlinelibrary.wiley.com/doi/10.1002/adfm.202101748

[42] D. Wang, L. Dong, G. Gu, 3D Printed Fractal Metamaterials with Tunable Mechanical Properties and Shape Reconfiguration, Advanced Functional Materials 33 (1) (2023) 2208849. doi:10.1002/ADFM.202208849.
URL https://onlinelibrary.wiley.com/doi/full/10.1002/adfm.202208849https://onlinelibrary.wiley.com/doi/abs/10.1002/adfm.202208849https://onlinelibrary.wiley.com/doi/10.1002/adfm.202208849

[43] B. Deng, A. Zareei, X. Ding, J. C. Weaver, C. H. Rycroft, K. Bertoldi, B. Deng, A. Zareei, X. Ding, J. C. Weaver, C. H. Rycroft, K. Bertoldi, Inverse Design of Mechanical Metamaterials with Target Nonlinear Response via a Neural Accelerated Evolution Strategy, Advanced Materials 34 (41) (2022) 2206238. doi:10.1002/ADMA.202206238.
URL https://onlinelibrary.wiley.com/doi/full/10.1002/adma.202206238https://onlinelibrary.wiley.com/doi/abs/10.1002/adma.202206238https://onlinelibrary.wiley.com/doi/10.1002/adma.202206238

[44] T. Xue, S. Adriaenssens, S. Mao, Learning the nonlinear dynamics of mechanical metamaterials with graph networks, International Journal of Mechanical Sciences 238 (2023) 107835. doi:10.1016/J.IJMECSCI.2022.107835.

[45] K. Guo, Z. Yang, C. H. Yu, M. J. Buehler, Artificial intelligence and machine learning in design of mechanical materials, Materials Horizons 8 (4) (2021) 1153–1172. doi:10.1039/D0MH01451F.
URL https://pubs.rsc.org/en/content/articlehtml/2021/mh/d0mh01451fhttps://pubs.rsc.org/en/content/articlelanding/2021/mh/d0mh01451f

[46] C. Imediegwu, R. Murphy, R. Hewson, M. Santer, Multiscale structural optimization towards three-dimensional printable structures, Structural and Multidisciplinary Optimization 60 (2) (2019) 513–525. doi:10.1007/S00158-019-02220-Y/FIGURES/14.
URL https://link.springer.com/article/10.1007/s00158-019-02220-y

[47] D. A. White, W. J. Arrighi, J. Kudo, S. E. Watts, Multiscale topology optimization using neural network surrogate models, Computer Methods in Applied Mechanics and Engineering 346 (2019) 1118–1135. doi:10.1016/j.cma.2018.09.007.
URL https://doi.org/10.1016/j.cma.2018.09.007

[48] M. Nightingale, R. Hewson, M. Santer, Multiscale optimisation of resonant frequencies for lattice-based additive manufactured structures, Structural and Multidisciplinary Optimization 63 (3) (2021) 1187–1201. doi:10.1007/S00158-020-02752-8/FIGURES/19.
URL https://link.springer.com/article/10.1007/s00158-020-02752-8

[49] G. Cerniauskas, P. Alam, Compressive properties of parametrically optimised mechanical metamaterials based on 3D projections of 4D geometries, Extreme Mechanics Letters (4 2023). doi:10.1016/j.eml.2023.102019.
URL https://linkinghub.elsevier.com/retrieve/pii/S2352431623000652
[50] G. Cerniauskas, P. Alam, Tensile properties of 3D projected 4-polytopes: a new class of mechanical metamaterialdoi:10.31224/2850.
URL https://engrxiv.org/preprint/view/2850
[51] Z. Yang, P. Alam, Designing Hierarchical Honeycombs to Mimic the Mechanical Behaviour of Composites, Journal of Composites Science 2021, Vol. 5, Page 17 5 (1) (2021) 17. doi:10.3390/JCS5010017.
URL https://www.mdpi.com/2504-477X/5/1/17/htmhttps://www.mdpi.com/2504-477X/5/1/17
[52] R. S. Farr, Y. Mao, Fractal space frames and metamaterials for high mechanical efficiency, EPL 84 (2008) 14001. doi:10.1209/0295-5075/84/14001.
URL www.epljournal.org
[53] Q. Chen, S. Huang, Mechanical properties of a porous bioscaffold with hierarchy, Materials Letters 95 (2013) 89–92. doi:10.1016/J.MATLET.2012.12.071.
[54] Z. Qin, G. S. Jung, M. J. Kang, M. J. Buehler, The mechanics and design of a lightweight three-dimensional graphene assembly, Science Advances 3 (1) (1 2017). doi:10.1126/SCIADV.1601536.
URL https://www.science.org
[55] M. Pelanconi, A. Ortona, Nature-inspired, ultra-lightweight structures with gyroid cores produced by additive manufacturing and reinforced by unidirectional carbon fiber ribs, Materials 12 (24) (2019) 1–14. doi:10.3390/ma1224134.
[56] C. Qi, F. Jiang, S. Yang, Advanced honeycomb designs for improving mechanical properties: A review, Composites Part B: Engineering 227 (12 2021). doi:10.1016/J.COMPOSITESB.2021.109393.
[57] J. M. Korde, M. Shaikh, B. Kandasubramanian, Bionic prototyping of honeycomb patterned polymer composite and its engineering application, Polymer - Plastics Technology and Engineering 57 (17) (2018) 1828–1844. doi:10.1080/03602559.2018.1434667.
URL https://www.tandfonline.com/action/journalInformation?journalCode=lpte21
[58] CEL COMPONENTS S.R.L., Polypropylene honeycomb core PP8-120T30 datasheet.
URL https://www.cel.eu/img_ins/files/poliprop_P880_Rev1_uk.pdf
[59] H. Yang, B. E. Abali, D. Timofeev, W. H. Müller, Determination of metamaterial parameters by means of a homogenization approach based on asymptotic analysis, Continuum Mechanics and Thermodynamics 32 (5) (2020) 1251–1270. doi:10.1007/s00161-019-00837-4.
[60] J. Bauer, L. R. Meza, T. A. Schaedler, R. Schwaiger, X. Zheng, L. Valdevit, Nanolattices: An Emerging Class of Mechanical Metamaterials, Advanced Materials 29 (2017) 1701850. doi:10.1002/adma.201701850.
URL https://onlinelibrary.wiley.com/doi/10.1002/adma.201701850
[61] Z. Qin, G. S. Jung, M. J. Kang, M. J. Buehler, The mechanics and design of a lightweight three-dimensional graphene assembly, Science Advances 3 (1) (1 2017). doi:10.1126/SCIADV.1601536.
URL https://www.science.org